

# Passivity-based Fractional-order Sliding-mode Control Design and Implementation of Grid-connected Photovoltaic Systems

Bo Yang <sup>1</sup>, Tao Yu <sup>2,3,\*</sup>, Hongchun Shu <sup>1</sup>, Dena Zhu <sup>1</sup>, Yiyan Sang <sup>4</sup>, Lin Jiang <sup>4</sup>

<sup>1</sup> Faculty of Electric Power Engineering, Kunming University of Science and Technology, 650500 Kunming, China;

<sup>2</sup> College of Electric Power, South China University of Technology, 510640 Guangzhou, China;

<sup>3</sup> Guangdong Key Laboratory of Clean Energy Technology, 510640 Guangzhou, China;

<sup>4</sup> Department of Electrical Engineering & Electronics, University of Liverpool, Liverpool, L69 3GJ, United Kingdom;

\* Correspondence: taoyu1@scut.edu.cn, Tel.: +86-130-020-88518

**Abstract:** In order to achieve the maximum power point tracking (MPPT) of Photovoltaic (PV) systems in the presence of time-varying stochastic operation conditions and various uncertainties/disturbances, a passivity-based fractional-order sliding-mode control (PbFoSMC) scheme is proposed. The design can be classified into two steps, i.e., (a) Construct a storage function in terms of the tracking error of DC-link voltage, DC-link current and q-axis current for the PV system, upon which the actual characteristics of each term is thoroughly analyzed. Moreover, the beneficial terms are carefully retained to enhance the dynamical responses of the closed-loop system while the detrimental terms are fully removed to realize a global control consistency; (b) Based on the passivized system, a fractional-order sliding-mode control (FoSMC) is incorporated as an additional input, which can considerably improve the control performance with the aim of rapid uncertainties/disturbances rejection. Four case studies, including the solar irradiance change, temperature variation, power grid voltage drop, and PV inverter parameter uncertainties, are undertaken to evaluate the effectiveness of PbFoSMC in comparison to that of PID control, passivity-based control (PBC), and sliding-mode control (SMC), respectively. At last, a dSpace based hardware-in-loop (HIL) test is carried out to validate the implementation feasibility of PbFoSMC.

**Keywords:** Photovoltaic system; MPPT; passivity-based fractional-order SMC; solar energy; HIL test

## Nomenclature

Variables		<i>R</i>	equivalent line resistance of the power grid
$V_{dc}$	PV output voltage	<i>L</i>	equivalent line inductance of the power grid
$I_{pv}$	PV output current	<i>C</i>	DC-link capacitance
$I_{ph}$	cell photocurrent	Abbreviations	
$I_s$	cell reverse saturation current	MPPT	maximum power point tracking
$I_{RS}$	d-q components of the grid current	PV	Photovoltaic
$T_c$	cell absolute working temperature, K	FRT	fault ride-through
$T_{ref}$	cell reference temperature, K	PO	perturb & observe
<i>S</i>	total solar irradiance, W/m <sup>2</sup>	SVPWM	space vector pulse width modulation
$E_g$	band-gap energy of the semiconductor used in the cell	PID	proportional-integral-derivative
$v_{d,q}$	d-q components of the output voltage of the inverter	FoPID	fractional-order PID
$e_{d,q}$	d-q components of the grid voltage	PBC	passivity-based control
$i_{d,q}$	cell reverse saturation current at reference solar irradiance and temperature	PbFoSMC	passivity-based fractional-order sliding-mode control
$\omega$	AC grid synchronous frequency	FLC	feedback linearization control
$N_p$	number of panels connected in parallel	SMC	sliding-mode control
$N_s$	number of panels connected in series	FoSMC	fractional-order sliding-mode control
PV system parameters		The PbFoSMC parameters	
<i>q</i>	electron charge, $1.60217733 \times 10^{-19}$ Cb	$\lambda_{ci}$	fractional-order PD <sup><math>\alpha</math></sup> sliding surface gain
<i>A</i>	p-n junction ideality factor, between 1 and 5	$\varphi_i, \varsigma_i$	fractional-order sliding-mode control gains
<i>k</i>	Boltzman constant, $1.380658 \times 10^{-23}$ J/K	$\epsilon_c$	thickness layer boundary of controller
$k_i$	cell short-circuit current temperature coefficient	$\alpha 1, \alpha 2$	operation order of fractional-order PD <sup><math>\alpha</math></sup> sliding surface
<i>R<sub>s</sub></i>	cell series resistance	$\kappa_i$	extra damping gains

## 1. Introduction

The astonishing booming of global population and fast industrialization of developing countries need to consume an enormous amount of energy. Currently, oil, gas and coal-based energy generation is the most commonly used resources which are however not sustainable due to their contribution to global warming and expected depletion

of reserves by years 2040, 2042 and 2112 respectively [1]. As a consequence, sustainable and inexhaustible renewable energy technologies for electricity generation are urgently required to fully satisfy the ever-growing energy demand, which is expected to generate about half of all growth over the period to 2040 [2]. Various technologies are developed to harvest energy from different renewable resources, such as solar, wind, hydropower, biofuel, geothermal, tidal, biomass [3]. Among which solar energy has gained numerous attentions and interests in both industry and academics thanks to its low operational costs and maintenance requirements, no moving parts, no carbon emissions and long lifetimes (more than 20 years) [4]. In addition, Photovoltaic (PV) systems have long lifetimes that makes them economically and technically feasible [5].

In practice, it is very crucial for the PV systems to always extract the available maximum solar power, which could be achieved by regulating the active power and operating the PV systems at the unity power factor, also well-known as maximum power point tracking (MPPT) [6]. Thus far, plenty of MPPT algorithms have been developed to dynamically adjust the power output of PV systems under various atmospheric conditions, e.g., hill-climbing [7], perturb & observe (P&O) [8], and incremental conductance (INC) [9]. When the maximum power point (MPP) is found, the DC-link voltage will be regulated by PV inverters to convert DC current into AC current for the integration into the main power grids or supporting local energy utilizers.

Therefore, a proper control system design of PV inverters is quite important to realize an effective and efficient MPPT. At present, vector control (VC) associated with proportional-integral-derivative (PID) loops have been widely used for the PV inverters due to its high operation reliability and structure simplicity [10]. Nevertheless, it cannot achieve a consistent control performance under various operation conditions as its control parameters are determined by local linearization, such scenarios are very common in PV systems operation as the weather conditions often change unpredictably. In order to improve the control performance of conventional PID control, reference [11] proposed a minimal-energy control strategy of an uncertain-parameter oriented PV system with the half-order PID controller. Meanwhile, optimal fractional-order PI (FoPI) controllers were developed for on-grid solar PV systems [12]. These approaches are based on fractional-order calculus which introduce two additional fractional-order parameters, such that the closed-loop system dynamics could be further tuned.

However, the above methods still own the inherent weakness of linear control, e.g., one-point linearization of the original nonlinear systems. In order to achieve a global control consistency, plenty of nonlinear control schemes are employed which aim to achieve a satisfactory control performance for different purposes. In work [13,14], feedback linearization control (FLC) was proposed for both the two-level and three-level grid-connected PV inverters, in which the PV inverter nonlinearities are fully removed to realize a global control consistency under various operation conditions. However, an accurate PV system model is required thus it is very sensitive to any parameter uncertainties or external disturbances. In addition, a backstepping MPPT controller of PV system under varying solar irradiance and temperature levels was designed to improve the tracking performance [15]. Besides, a model predictive control (MPC) was developed for PV sources in a smart DC distribution system to achieve MPPT and droop control [16]. Moreover, reference [17] presented an enhanced forced switching sliding mode control (FSSMC) scheme to reject uncertainties and disturbances, which can significantly enhance the robustness of PV system and was implemented by an experimental prototype. In literature [18], a disturbance estimator was used for the digital predictive current controller, which can minimize its sensitivity against parameter uncertainties and can rapidly reject grid-side disturbances.

Generally speaking, the above strategies regard the PV system control as a mathematical problem while the physical properties are somehow ignored or not fully analyzed, which are actually quite crucial and meaningful for the dynamical responses of a physical system. Based on the Lyapunov theory, passivity offers an invaluable insight of physical features of engineering problems that treats a dynamical system as a virtual energy-transformation device. It is able to flexibly decompose a complex/complicated original system into several simpler subsystems that, upon appropriate interconnections, and add up their local/distributed energies to desirably reshape the overall energy of the closed-loop systems' behaviour described by a storage function [19]. In particular, the action of a controller connected to the dynamical system could also be viewed, in terms of energy, as another separate dynamical system. Therefore, the control problems are equalized to construct a proper interconnection pattern between the controller and the dynamical system, such that the real-time variations of the storage function can take a preferable form [20]. Hence, passivity-based control (PBC) is quite promising for PV control system design as it can be considered as an energy-transformation device, e.g., the solar energy is transformed into DC current (PV cells/arrays) and then converted into AC current (PV inverters). In reference [21], a passivity-based MPPT controller was devised for grid-connected PV systems, which can achieve a rapid and accurate PV system response to the variations of external environment conditions. Furthermore, PBC was synthesized via the energy shaping and damping injection techniques for power management of PV/battery hybrid power sources [22]. Meanwhile, an adaptive passivity-based controller (APBC) was developed for PV/battery hybrid power sources via an algebraic parameter identifier, which can estimate the unknown parameters of PV array voltage, battery voltage, and load resistance [23]. In work [24], a PBC was

designed for T-type neutral point clamped (T-NPC) PV inverter with Euler-Lagrange (EL) representation by the damping injection method, such that the dynamical performance of the current connected into the power grid can be dramatically improved. In addition, a PBC was used for PV inverter to ensure global asymptotic convergence of the tracking error to zero and the PV inverter shows robust current tracking with fast dynamics [25].

One significant drawback of PBC is the requirement of an accurate system upon which the physical properties of each term could be analyzed. In order to remedy this inherent flaw, this paper proposes a novel passivity-based fractional-order SMC (PbFoSMC) scheme of PV systems for MPPT under different atmospheric conditions. A storage function is firstly constructed, in which the physical properties of each terms are thoroughly investigated and fully exploited. Then, a fractional-order SMC (FoSMC) framework [26,27] is synthesized as the additional input of the passivized system to desirably reshape the storage function, as well as considerably enhance the robustness of the closed-loop system in the presence of PV inverter parameter uncertainties. Therefore, the elegant advantages of optimality of PBC and robustness of FoSMC could be wisely incorporated. Comprehensive case studies are undertaken to evaluate the control performance of PbFoSMC in comparison to other typical controllers. Lastly, a dSpace based hardware-in-loop (HIL) is carried out to validate the implementation feasibility of the proposed approach.

The remaining of this paper is organized as follows: Section 2 presents the grid-connected PV inverter model; In Section 3, the methodology of PBC and FoSMC are briefly introduced; Besides, Section 4 designs the PbFoSMC of PV for MPPT. Case studies are undertaken in Section 5 while dSpace based HIL tests are given in Section 6. Lastly, Section 7 summarizes the concluding marks of the whole paper.

## 2. Grid-connected PV Inverter Modelling

The structure of a grid-connected PV inverter is shown in Fig. 1, which includes a PV array, capacitive DC link, a PV inverter, and a three-phase power grid. Here, the PV array attempts to convert the solar irradiance into the DC current, while the DC-link capacitors reduce the high frequency ripple of the DC voltage in the input side of the PV inverter [6].

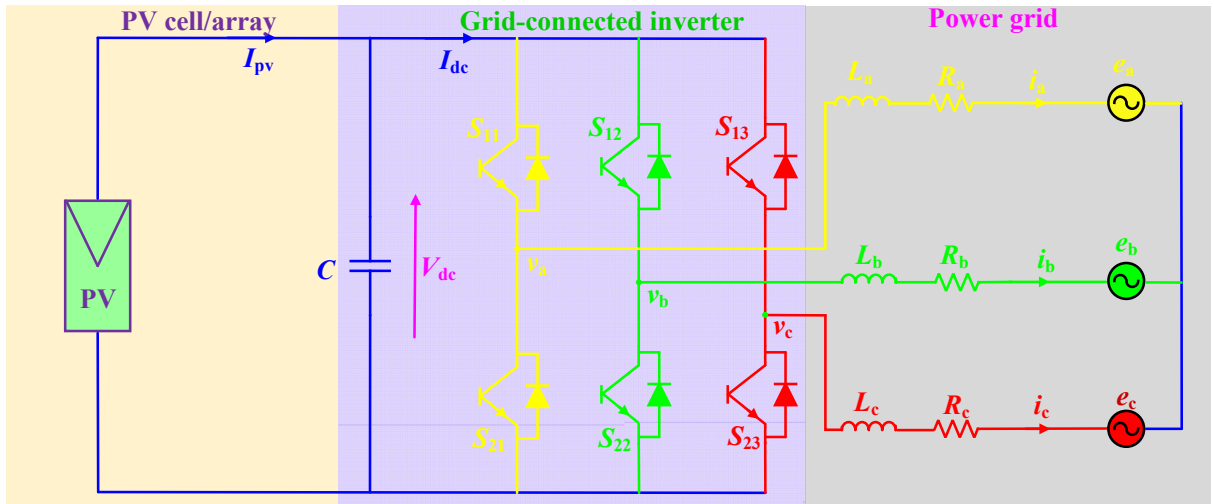


Figure 1. The structure of a grid-connected PV inverter.

### 2.1. PV array model

A PV cell is generally a p-n semiconductor junction diode which converts the solar irradiance into the electricity, while its equivalent circuit is provided by Fig. 2. It consists of a light generated current source, a parallel diode, and a series resistance, respectively. Generally, PV cells are grouped together to form PV modules, which are combined in both series and parallel to provide a desired output power [6]. Denote the number of PV cells in series and in parallel to be  $N_s$  and  $N_p$ , respectively, the relationship between the output current and voltage can be described by [13,14]

$$I_{pv} = N_p I_{ph} - N_p I_s \left( \exp \left[ \frac{q}{AKT_c} \left( \frac{V_{dc}}{N_s} + \frac{R_s I_{pv}}{N_p} \right) \right] - 1 \right) \quad (1)$$

where the meaning of each symbol is given in Nomenclature.

The generated photocurrent  $I_{ph}$  is determined by the solar irradiance, as follows

$$I_{ph} = (I_{sc} + k_i(T_c - T_{ref})) \frac{s}{1000} \quad (2)$$

Moreover, the PV cell saturation current  $I_s$  changes with the temperature based on the following relationship:

$$I_s = I_{RS} \left[ \frac{T_c}{T_{ref}} \right]^3 \exp \left[ \frac{qE_g}{Ak} \left( \frac{1}{T_{ref}} - \frac{1}{T_c} \right) \right] \quad (3)$$

The reverse saturation current at the rated solar irradiance and temperature is approximated as

$$I_s = \frac{I_{sc}}{\exp\left(\frac{qV_{oc}}{N_s k A T_c}\right) - 1} \quad (4)$$

The above equations (1)-(4) indicate that the current generated by the PV array is simultaneously relied on the solar irradiance and temperature. Here, a PV array of 30 panels in series is employed while each module contains 36 cells in series [13]. respectively.

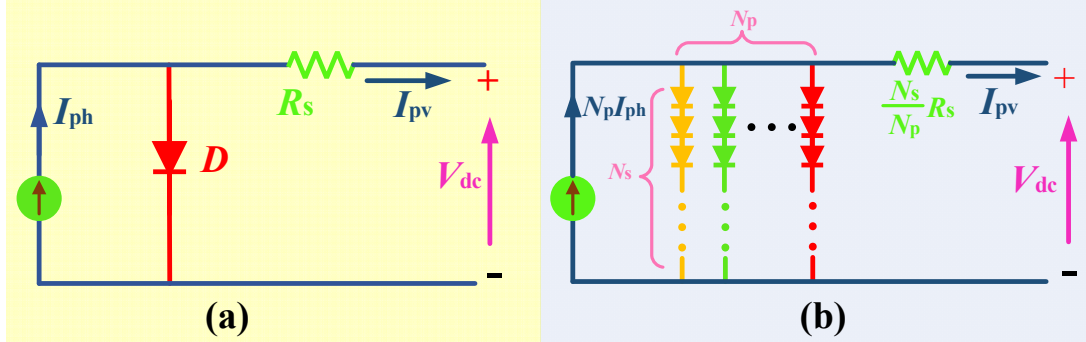


**Figure 2.** Equivalent circuit of PV cell/array circuit. (a) Single cell circuit; (b) PV array circuit with  $N_s$  in series and  $N_p$  in parallel.

## 2.2 PV inverter model

Only the balanced conditions are considered, e.g., three phases have identical parameters and their voltages and currents have the same amplitude while each phase shifts  $120^\circ$  between themselves [13,14]. Based on the Park's transformation, the PV inverter dynamics is transformed from the stationary  $abc$  frame into the synchronous rotating  $dq$  frame, as follows [28,29]

$$\begin{cases} v_d = e_d + R i_d + L \frac{di_d}{dt} + \omega L i_q \\ v_q = e_q + R i_q + L \frac{di_q}{dt} - \omega L i_d \end{cases} \quad (5)$$

where  $e_d$ ,  $e_q$ ,  $i_d$ ,  $i_q$ ,  $v_d$ , and  $v_q$  denote the dq-axis components of grid voltage, grid current, and PV inverter output voltage, respectively;  $R$  and  $L$  represent the equivalent resistance and inductance, respectively; while  $\omega$  denotes the AC grid synchronous frequency. Ignore the power losses in PV inverter switches, the power balance relationship between the DC input side and the AC output side can be described as

$$e_d i_d + e_q i_q = V_{dc} I_{dc} \quad (6)$$

where  $V_{dc}$  and  $I_{dc}$  are the input voltage and current of the PV inverter, respectively. It is worth noting that output voltage  $V_{dc}$  and output current  $I_{pv}$  are actually the voltage at maximum power ( $V_{pm}$ ) and the current at maximum power ( $I_{pm}$ ), respectively.

The dynamics of the DC side is obtained by applying Kirchhoff's current law, as follows

$$C \frac{dV_{dc}}{dt} = I_{pv} - I_{dc} = I_{pv} - \frac{e_d i_d + e_q i_q}{V_{dc}} \quad (7)$$

where  $C$  is the DC bus capacitance.

## 2.3 Perturb and observe (P&O) based MPPT

This paper merely considers the uniform solar irradiance condition, e.g., there exists no partial shading effect. Hence, the  $P$ - $V$  curve of PV module has only one peak. Here, P&O technique [8] is adopted to efficiently track the maximum power point (MPP) under fast varying atmospheric conditions, which operates by periodically incrementing or decrementing the output voltage of the PV cell and compares the power obtained in the current cycle with the power of the previous one. Basically, P&O method measures the derivative of PV cell power ( $dP$ ) and derivative of PV cell voltage ( $dV$ ) and uses PV power-voltage curve to determine the movement of the operation point. In particular, if the sign of ( $dP/dV$ ) is positive, then the actual point is at the left side of MPP; else ( $dP/dV$ ) is negative, then the actual point is at the right side of MPP. Such process continues until ( $dP/dV$ ) equals to zero, as shown in Fig. 3.

$$\begin{cases} \frac{dP}{dV} = 0 \Rightarrow \text{MPP} \\ \frac{dP}{dV} > 0 \Rightarrow \text{Left side of MPP} \\ \frac{dP}{dV} < 0 \Rightarrow \text{Right side of MPP} \end{cases} \quad (8)$$

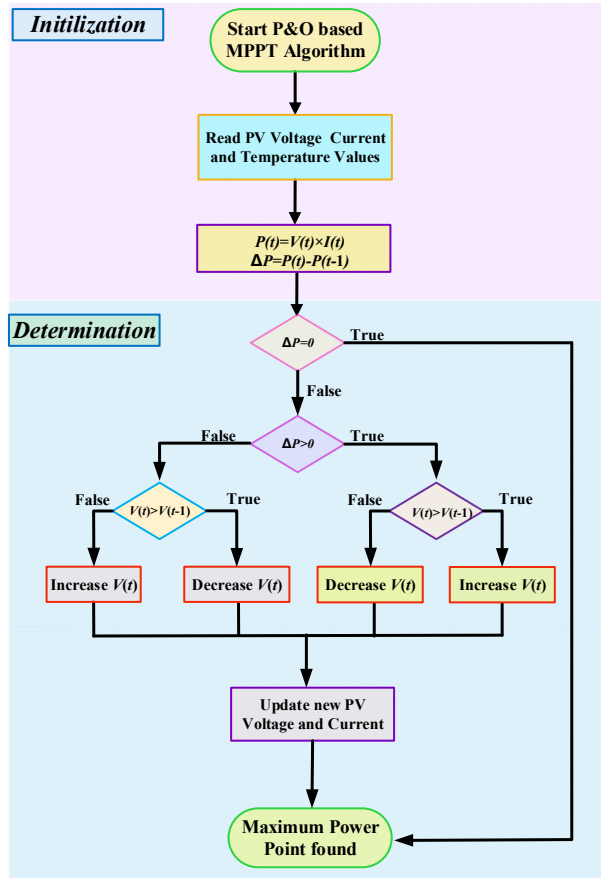


Figure 3. Flowchart of P&O based MPPT algorithm.

### 3 Methodologies

#### 3.1 Passivity-based control

Consider a dynamical nonlinear system represented with the following general model

$$\begin{cases} \dot{x} = f(x, u) \\ y = h(x, u) \end{cases} \quad (9)$$

where  $x \in \mathcal{R}^n$  is the system state vector.  $u \in \mathcal{R}^m$  and  $y \in \mathcal{R}^m$  represent the input and output, respectively.

The energy balancing can be written as follows [19,20]:

$$\underbrace{H[x(t)] - H[x(0)]}_{\text{stored}} = \underbrace{\int_0^t u^T(s)y(s)ds}_{\text{supplied}} - \underbrace{d(t)}_{\text{dissipated}} \quad (10)$$

where  $H(x)$  is the storage function, and  $d(t)$  is a nonnegative function that characterizes the dissipation effects in practical engineering problems, such as friction and heat. Undoubtedly, energy balancing is a universal property of physical systems, which captures a very broad range of applications that include nonlinear and time-varying dynamics.

System (9) is defined to be output strictly passive if there exists a continuously differentiable positive semi-definite function  $H(x)$ , such that

$$u^T y \geq \frac{\partial H}{\partial x} f(x, u) + \zeta y^T y, \forall (x, u) \in \mathcal{R}^n \times \mathcal{R}^m \quad (11)$$

where  $\zeta > 0$ . In order to obtain the asymptotic stability, the following Lemma 1 is needed.

**Lemma 1** [19]. *Consider system (9). The origin of the uncontrolled system  $\dot{x} = f(x, 0)$  is asymptotically stable if the system is output strictly passive and zero-state detectable with a positive definite storage function  $H(x)$ . Moreover, if the storage function  $H(x)$  is radially unbounded then the origin is globally asymptotically stable.*

If system (9) is not passive, but there exists a positive definite storage function  $H(x)$  and a feedback control law  $u = \beta(x) + kv$  such that  $\dot{H} \leq vy$ , then the feedback system is passive. As a result, the feedback passivation can be used as a preliminary step in a stabilization design due to the additional output feedback

$$v = -\phi(y) \quad (12)$$

where  $\phi(y)$  is a sector-nonlinearity satisfying  $y\phi(y) > 0$  for  $y \neq 0$  and  $\phi(0)=0$ , can achieve  $\dot{H} \leq -y\phi(y) \leq 0$ .

As shown in Fig. 4, the controller,  $\Sigma_C$ , is treated as a one-port system that will be coupled with the plant to be controlled,  $\Sigma_P$ , via a two-port interconnection subsystem,  $\Sigma_I$ . More details of PBC can be referred to literatures [19,20]



for interested readers.

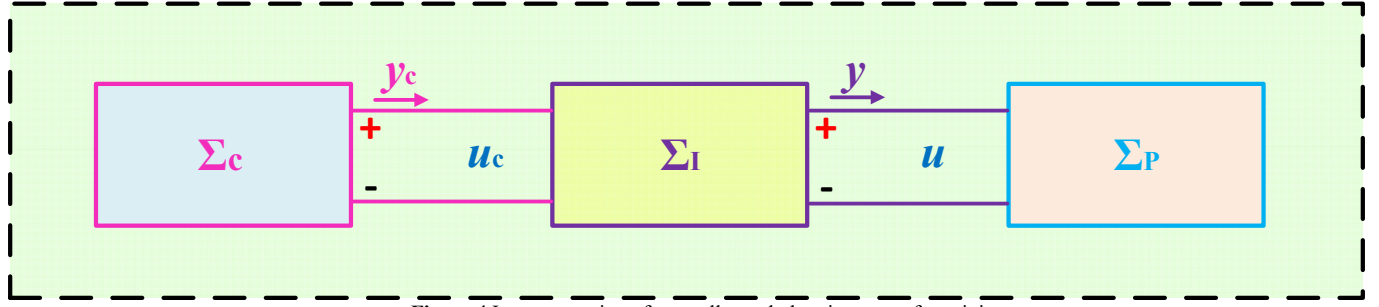


Figure 4 Interconnection of controller and plant in terms of passivity.

### 3.2 Fractional-order SMC

Fractional-order calculus is a generalization of integration and differentiation to non-integer order domain, the fundamental operator  ${}_a D_t^\alpha$  is defined as [26]

$${}_a D_t^\alpha = \begin{cases} \frac{d^\alpha}{dt^\alpha}, & \alpha > 0 \\ 1, & \alpha = 0 \\ \int_a^t (d\tau)^{-\alpha}, & \alpha < 0 \end{cases} \quad (13)$$

where  $a$  and  $t$  are the lower and upper limits while  $\alpha \in \mathcal{R}$  is the operation order.

Here, one of the commonly used definition of fractional-order derivative, e.g., Caputo definition, is used with *Gamma* function, as

$${}_a D_t^\alpha f(t) = \frac{1}{\Gamma(n-\alpha)} \int_a^t \frac{f^{(n)}(\tau)}{(t-\tau)^{\alpha-n+1}} d\tau \quad (14)$$

where  $n$  is the first integer which is not less than  $\alpha$ , e.g.,  $n-1 \leq \alpha < n$ .  $\Gamma(\cdot)$  is the *Gamma* function.

The Laplace transformation of the Caputo fractional-order derivative (15) is written by

$$\int_0^\infty {}_0 D_t^\alpha f(t) e^{-st} dt = s^\alpha \mathcal{L}\{f(t)\} - \sum_{k=0}^{n-1} s^{\alpha-k-1} f^{(k)}(0) \quad (15)$$

where  $\mathcal{L}\{\cdot\}$  is the Laplace operator. As a result, under the zero initial conditions, the fractional integral operator with order  $\alpha$  can be represented by the transfer function  $F(s) = 1/s^\alpha$  in the frequency domain.

As it is quite challenging to obtain the exact solution of fractional differential equations, it is often approximated in the frequency domain. Besides, the transfer functions containing the fractional powers of  $s$  are approximated with usual (integer-order) transfer functions and a similar behaviour. Here, the Oustaloup approximation [27] is adopted for a recursive distribution of poles and zeroes, as follows

$$s^\alpha \approx K \prod_{n=-N}^N \frac{1 + \left(\frac{s}{\omega_{z,n}}\right)}{1 + \left(\frac{s}{\omega_{p,n}}\right)}, \quad \alpha > 0 \quad (16)$$

where  $2N+1$  is the number of poles and zeros chosen beforehand,  $K$  is the gain which makes both sides of Eq. (16) to have unit gain at 1 rad/s.  $\omega_{z,n}$  and  $\omega_{p,n}$  are given as

$$\omega_{z,n} = \omega_b \left(\frac{\omega_h}{\omega_b}\right)^{(n+N+(1-\alpha)/2)/(2N+1)} \quad (17)$$

$$\omega_{p,n} = \omega_b \left(\frac{\omega_h}{\omega_b}\right)^{(n+N+(1+\alpha)/2)/(2N+1)} \quad (18)$$

In Eq. (17) and (18),  $\omega_b$  and  $\omega_h$  represent the lower and upper limits of frequency of approximation, respectively. Normally it has  $\omega_b \omega_h = 1$  and  $k = \omega_h^\alpha$ .

The stability of fractional-order system is guaranteed in Lemma 2.

**Lemma 2** [30]. Consider the following autonomous system:

$${}_0 D_t^\alpha z = Cz, \quad z(0) = z_0 \quad (19)$$

where  $z \in \mathcal{R}^n$  and  $C \in \mathcal{R}^{n \times n}$  are asymptotically stable if  $|\arg(\text{eig}(C))| > \alpha\pi/2$ , in which each component of the states decays towards 0 like  $t^{-\alpha}$ . Moreover, system (19) is stable if  $|\arg(\text{eig}(C))| \geq \alpha\pi/2$  with those critical eigenvalues satisfying  $|\arg(\text{eig}(C))| = \alpha\pi/2$  have geometric multiplicity one.

Define a fractional-order PD $^\alpha$  sliding surface for system (9) as

$$S_{FO} = D^\alpha(x_1 - y_d) + \lambda_c(x_1 - y_d) \quad (20)$$

where positive constant  $\lambda_c$  denotes the fractional-order PD $^\alpha$  sliding surface gain.

Let  $S_{FO} = 0$ , it yields

$$D^\alpha(x_1 - y_d) = -\lambda_c(x_1 - y_d) \quad (21)$$

According to Lemma 2, it obtains that  $C = -\lambda_c$  and  $|\arg(\text{eig}(C))| = \pi$ . When  $0 < \alpha < 2$ ,  $|\arg(\text{eig}(C))| > \alpha\pi/2$  can be constantly established. As a result, the dynamics of fractional-order  $\text{PD}^\alpha$  sliding surface (20) is asymptotically stable.

#### 4 PbFoSMC Design of PV Inverter for MPPT

Define the tracking error  $e = [e_1, e_2]^T = [i_q - i_q^*, V_{dc} - V_{dc}^*]^T$ , where  $i_q^*$  and  $V_{dc}^*$  are the references of q-axis current and DC-link voltage, respectively. Differentiate the tracking error  $e$  until the control input  $u$  appears explicitly, yields

$$\begin{bmatrix} \dot{e}_1 \\ \dot{e}_2 \end{bmatrix} = \begin{bmatrix} f_1(x) \\ f_2(x) \end{bmatrix} + B(x) \begin{bmatrix} u_1 \\ u_2 \end{bmatrix} - \begin{bmatrix} \dot{i}_q^* \\ \dot{V}_{dc}^* \end{bmatrix} \quad (22)$$

where

$$\begin{cases} f_1(x) = -\frac{R}{L}i_q + \omega i_d - \frac{e_q}{L} \\ f_2(x) = \frac{i_{pv}}{C} - \frac{e_d(-\frac{R}{L}i_d - \omega i_q - \frac{e_d}{L}) + e_q(-\frac{R}{L}i_q + \omega i_d - \frac{e_q}{L})}{CV_{dc}} - \frac{(e_d i_d + e_q i_q)}{C^2 V_{dc}^2} I_{pv} + \frac{(e_d i_d + e_q i_q)^2}{C^2 V_{dc}^3} \end{cases} \quad (23)$$

with

$$B(x) = \begin{bmatrix} 0 & \frac{1}{L} \\ -\frac{e_d}{LCV_{dc}} & -\frac{e_q}{LCV_{dc}} \end{bmatrix} \quad (24)$$

In order to ensure the above input-output linearization to be valid, the control gain matrix  $B(x)$  must be nonsingular among the whole operation range, which requires

$$\det[B(x)] = \frac{e_d}{L^2 CV_{dc}} \neq 0 \quad (25)$$

Since the grid voltage component  $e_d$  is always different from zero, the above condition can be constantly satisfied.

A storage function of tracking error dynamics (22) is constructed as

$$H(i_q, V_{dc}, I_{dc}) = \underbrace{\frac{1}{2}(i_q - i_q^*)^2}_{\text{AC series-resistor heat}} + \underbrace{\frac{1}{2}(V_{dc} - V_{dc}^*)^2}_{\text{DC parallel-resistor heat}} + \underbrace{\frac{1}{2}\left(\frac{I_{dc}}{C} - \dot{V}_{dc}^*\right)^2}_{\text{DC series-resistor heat}} \quad (26)$$

Here, the storage function  $H(i_q, V_{dc}, I_{dc})$  is consisted of the sum of heat produced by q-axis current  $i_q$  on a virtual unit AC series-resistor, the heat produced by DC-link voltage  $V_{dc}$  across a virtual unit DC parallel-resistor, as well as the heat generated by DC-link current  $I_{dc}$  flowing through a virtual unit DC series-resistor, respectively.

Furthermore, The first term of storage function (26), e.g.,  $\frac{1}{2}(i_q - i_q^*)^2$ , attempts to regulate the power factor; While the latter two terms, e.g.,  $\frac{1}{2}(V_{dc} - V_{dc}^*)^2$  and  $\frac{1}{2}\left(\frac{I_{dc}}{C} - \dot{V}_{dc}^*\right)^2$ , can be treated as an energy transformation from the solar energy into electricity. This can be interpreted as the changes of PV output power  $I_{pv}$  are determined by the variation of DC-link voltage  $V_{dc}$  and DC-link current  $I_{dc}$  according to relationship (7).

**Remark 1.** Note that the tracking error and storage function  $H$  only include the q-axis current  $i_q$  and DC-link voltage  $V_{dc}$  while d-axis current  $i_d$  is excluded. This is due to the reason that MPPT is achieved by regulating DC-link voltage  $V_{dc}$  (with relative degree of 2); Meanwhile, another goal is to regulate the reactive power which is determined by the q-axis current  $i_q$  in the chosen alignment framework (with relative degree of 1). As there are only two inputs, e.g.,  $u_1$  and  $u_2$ , and the overall order of tracking error dynamics (22) is 3, they are fully used to achieve the above two goals (2+1=3) and no more input could be adopted for the regulation of d-axis current  $i_d$ . However, based on the relationship (5)-(7), d-axis current will be indirectly regulated after the q-axis current and DC-link voltage are all controlled.

**Remark 2.** The third term of storage function  $H$ , e.g.,  $\frac{1}{2}\left(\frac{I_{dc}}{C} - \dot{V}_{dc}^*\right)^2$  is actually  $\frac{1}{2}(\dot{V}_{dc} - \dot{V}_{dc}^*)^2$ . This can be directly obtained from the relationship  $C \frac{dV_{dc}}{dt} = I_{dc}$ . The reason this paper does not directly use their derivative but indirectly use their equivalent relationship is to provide a clearer physical representation of these two terms. Particularly, one can readily find the DC-link current  $I_{dc}$  and DC-link capacitor  $C$  of the storage function  $H$  as they can be directly measured/obtained in practice.

Differentiate storage function (26) with respect to the time, gives

$$\dot{H}(i_q, V_{dc}, I_{dc}) = (i_q - i_q^*) \left( -\frac{R}{L} i_q + \omega i_d - \frac{e_q}{L} + \frac{1}{L} u_2 - i_q^* \right) + \left( \frac{I_{dc}}{C} - \dot{V}_{dc}^* \right) \left[ V_{dc} - V_{dc}^* + \frac{i_{pv}}{C} - \frac{e_d \left( -\frac{R}{L} i_d - \omega i_q - \frac{e_d}{L} \right) + e_q \left( -\frac{R}{L} i_q + \omega i_d - \frac{e_q}{L} \right)}{C V_{dc}} - \frac{(e_d i_d + e_q i_q)}{C^2 V_{dc}^3} I_{pv} + \frac{(e_d i_d + e_q i_q)^2}{C^2 V_{dc}^3} - \frac{e_d}{L C V_{dc}} u_1 - \frac{e_q}{L C V_{dc}} u_2 - \dot{V}_{dc}^* \right] \quad (27)$$

Design PbFoSMC for system (22) as

$$\begin{cases} u_1 = -\frac{L C V_{dc}}{e_d} [\ddot{V}_{dc}^* - V_{dc} + V_{dc}^* + \frac{e_q}{L C V_{dc}} u_2 - \frac{i_{pv}}{C} + \frac{e_d \left( -\frac{R}{L} i_d - \omega i_q - \frac{e_d}{L} \right) + e_q \left( -\frac{R}{L} i_q + \omega i_d - \frac{e_q}{L} \right)}{C V_{dc}} + \frac{(e_d i_d + e_q i_q)}{C V_{dc}^2} \dot{V}_{dc}^* + v_1] \\ u_2 = L \dot{i}_q^* - \omega L i_d + R i_q^* + e_q + v_2 \end{cases} \quad (28)$$

where  $v_1$  and  $v_2$  denote the additional inputs. Substitute PbFoSMC (28) into the derivative of storage function (27), together with the DC-link relationship (7), yields

$$\dot{H}(i_q, V_{dc}, I_{dc}) = \underbrace{-\frac{1}{C R_{dc}} (\dot{V}_{dc} - \dot{V}_{dc}^*)^2 - \frac{R}{L} (i_q - i_q^*)^2}_{\text{beneficial terms retainment}} + \underbrace{(\dot{V}_{dc} - \dot{V}_{dc}^*) v_1 + \frac{i_q - i_q^*}{L} v_2}_{\text{additional inputs}} \quad (29)$$

where  $R_{dc} = \frac{V_{dc}^2}{e_d i_d + e_q i_q}$  can be regarded as a virtual resistor in parallel with DC-link capacitor.

The fractional-order PD $^\alpha$  sliding surface of tracking error dynamics (22) is chosen as

$$\begin{bmatrix} S_{FO1} \\ S_{FO2} \end{bmatrix} = \begin{bmatrix} D^{\alpha_1} (i_q - i_q^*) + \lambda_{c1} (i_q - i_q^*) \\ D^{\alpha_2} (V_{dc} - V_{dc}^*) + \lambda_{c2} (V_{dc} - V_{dc}^*) \end{bmatrix} \quad (30)$$

where  $\alpha_1$  and  $\alpha_2$  denote the operation orders while positive gains  $\lambda_{c1}$  and  $\lambda_{c2}$  represent the fractional-order PD $^\alpha$  sliding surface gains, respectively. The attractiveness of fractional-order PD $^\alpha$  sliding surface (30) guarantees the convergence of the tracking error of q-axis current  $i_q$  and DC link voltage  $V_{dc}$ .

The additional inputs are then designed as

$$\begin{cases} v_1 = \underbrace{-\kappa_1 (i_q - i_q^*)}_{\text{extra damping}} \underbrace{-\zeta_1 S_{FO1} - \varphi_1 \text{sat}(S_{FO1}, \epsilon_{c1})}_{\text{robustness enhancement}} \\ v_2 = \underbrace{-\kappa_2 (V_{dc} - V_{dc}^*)}_{\text{extra damping}} \underbrace{-\zeta_2 S_{FO2} - \varphi_2 \text{sat}(S_{FO2}, \epsilon_{c2})}_{\text{robustness enhancement}} \end{cases} \quad (31)$$

where positive constants  $\zeta_1, \zeta_2, \varphi_1$ , and  $\varphi_2$  are the fractional-order PD $^\alpha$  sliding surface gains which are chosen to ensure the convergence of tracking error dynamics (22).  $\text{sat}(\cdot)$  function is used to replace the  $\text{sgn}(\cdot)$  function to reduce the malignant effect of chattering in conventional SMC, in which  $\epsilon_{c1}$  and  $\epsilon_{c2}$  represents the thickness layer. In addition, positive gains  $\kappa_1$  and  $\kappa_2$  are employed to inject extra damping of the closed-loop system, such that an improved dynamical responses could be resulted in.

Here, the first two terms of system (29) are carefully retained as they are beneficial terms of the PV system, which can accelerate the error tracking rate of q-axis current  $i_q$  and DC-link voltage  $V_{dc}$ . Meanwhile, the last two terms of system (29) are incorporated with additional inputs (30) and (31), which is designed to achieve the following two goals:

- *Extra damping*: Desirably accelerate the energy dissipation rate to achieve a rapid tracking through the first terms, e.g.,  $-\kappa_1 (i_q - i_q^*)$  and  $-\kappa_2 (V_{dc} - V_{dc}^*)$ ;
- *Robustness enhancement*: Provide considerable robustness against various PV modelling uncertainties and external disturbances, together with enhanced control performance by the use of fractional-order PD $^\alpha$  sliding surface (30).

To this end, the overall control structure of PbFoSMC control (28), (30) and (31) for PV system (1)-(7) to achieve MPPT is illustrated by Fig. 5, in which the control inputs are modulated by the space vector pulse width modulation (SVPWM) [31].

**Remark 3.** The conventional linear PI/PID control scheme employs an inner current-loop to regulate the inverter current to avoid overcurrent. In contrast, the proposed PbFoSMC scheme is a nonlinear strategy which actually contains no inner current-loop in its control law while it cannot handle the overcurrent. Hence, the overcurrent protection devices [32] will be activated to prevent the overcurrent to grow.



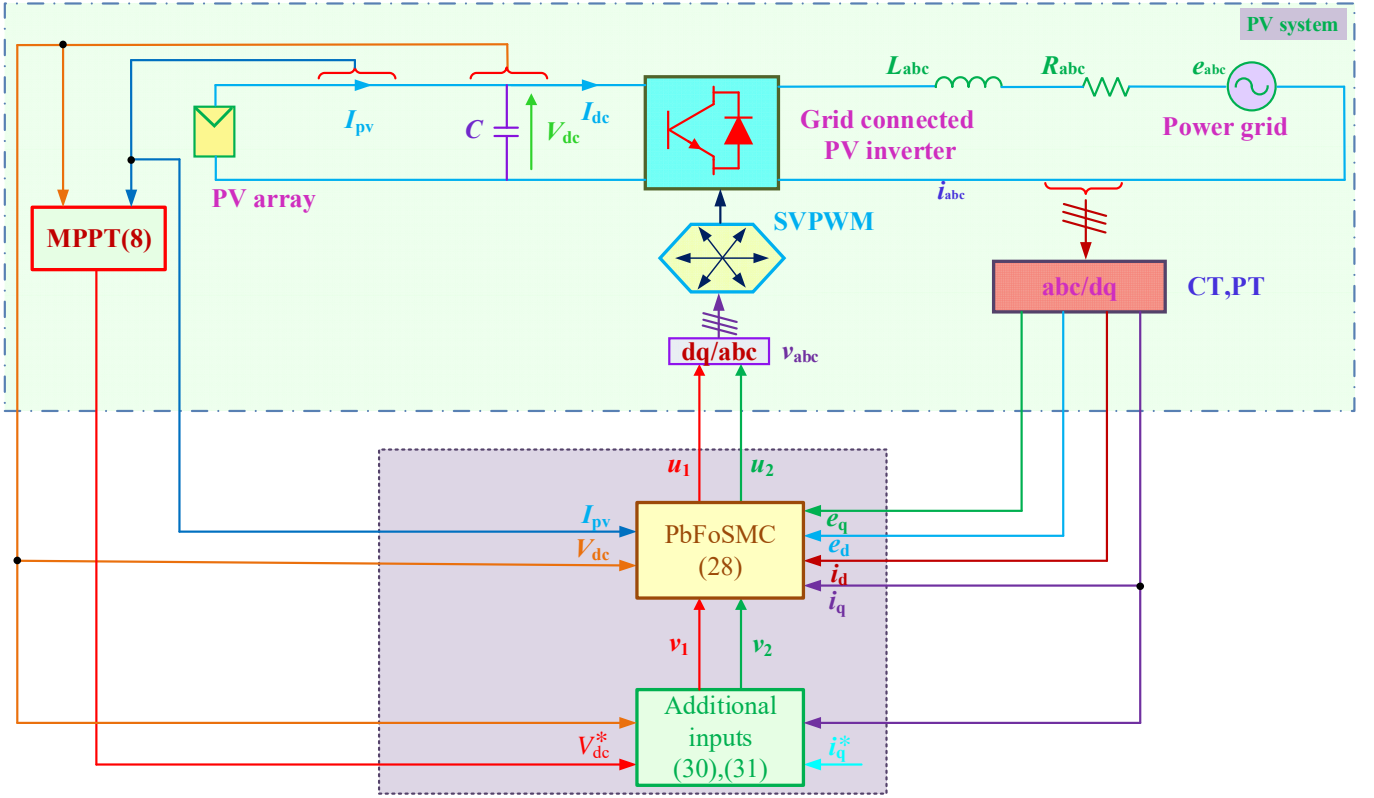


Figure 5. The overall PbFoSMC structure of the grid connected PV inverter for MPPT.

## 5. Case Studies

In order to evaluate the control performance of PbFoSMC under different weather conditions, three typical control schemes, e.g., PID control [10], PBC [21], and SMC [17], are adopted and compared under the following four cases, e.g., (a) Solar irradiance change; (b) Temperature variation; (c) Power grid voltage drop; and (d) PV inverter parameter uncertainties, whose control parameters are taken from the corresponding references, respectively. In addition, since the control inputs may exceed the admissible capacity of the PV inverter at some operation points, their values are bounded in  $[-0.6, 0.6]$  per unit (p.u.). Besides, Table 1 and Table 2 tabulate the PV system parameters taken from reference [13] and PbFoSMC parameters determined through trial-and-error.

Moreover, the initial solar irradiance and temperature are set at their rated values, e.g.,  $1 \text{ kW/m}^2$  and  $25^\circ\text{C}$ , together with the q-axis current  $I_q=0$ . Under such standard conditions, the PV output power  $P=1867 \text{ W}$ , DC link voltage  $V_{dc}=539.5 \text{ V}$ , and PV output current  $I_{pv}=3.46 \text{ A}$ , respectively. Lastly, all the case studies are carried out by simulation using Matlab/Simulink 2016a with a personal computer with an Intel<sup>R</sup> CoreTMi7 CPU at 2.2 GHz and 8 GB of RAM. The solver is ode 4 (Runge-Kutta) with a fixed-step size of  $10^{-4}$ .

Table 1. The PV system parameters

Typical peak power	60W	Factor of PV technology (A)	1.5
Voltage at peak power	17.1V	Series resistance	$0.21\Omega$
Current at peak power	3.5A	Grid voltage (V:rms)	120V
Short-circuit current ( $I_{sc}$ )	3.8A	Grid frequency (f)	50Hz
Open-circuit voltage ( $V_{oc}$ )	21.1V	Grid inductance line (L)	2mH
Temperature coefficient of $I_{sc}$ ( $k_1$ )	$3\text{mA}/^\circ\text{C}$	Grid resistor line (R)	$0.1\Omega$
Nominal operation cell temperature ( $T_{ref}$ )	$49^\circ\text{C}$	DC bus capacitor(C)	$2200\mu\text{F}$

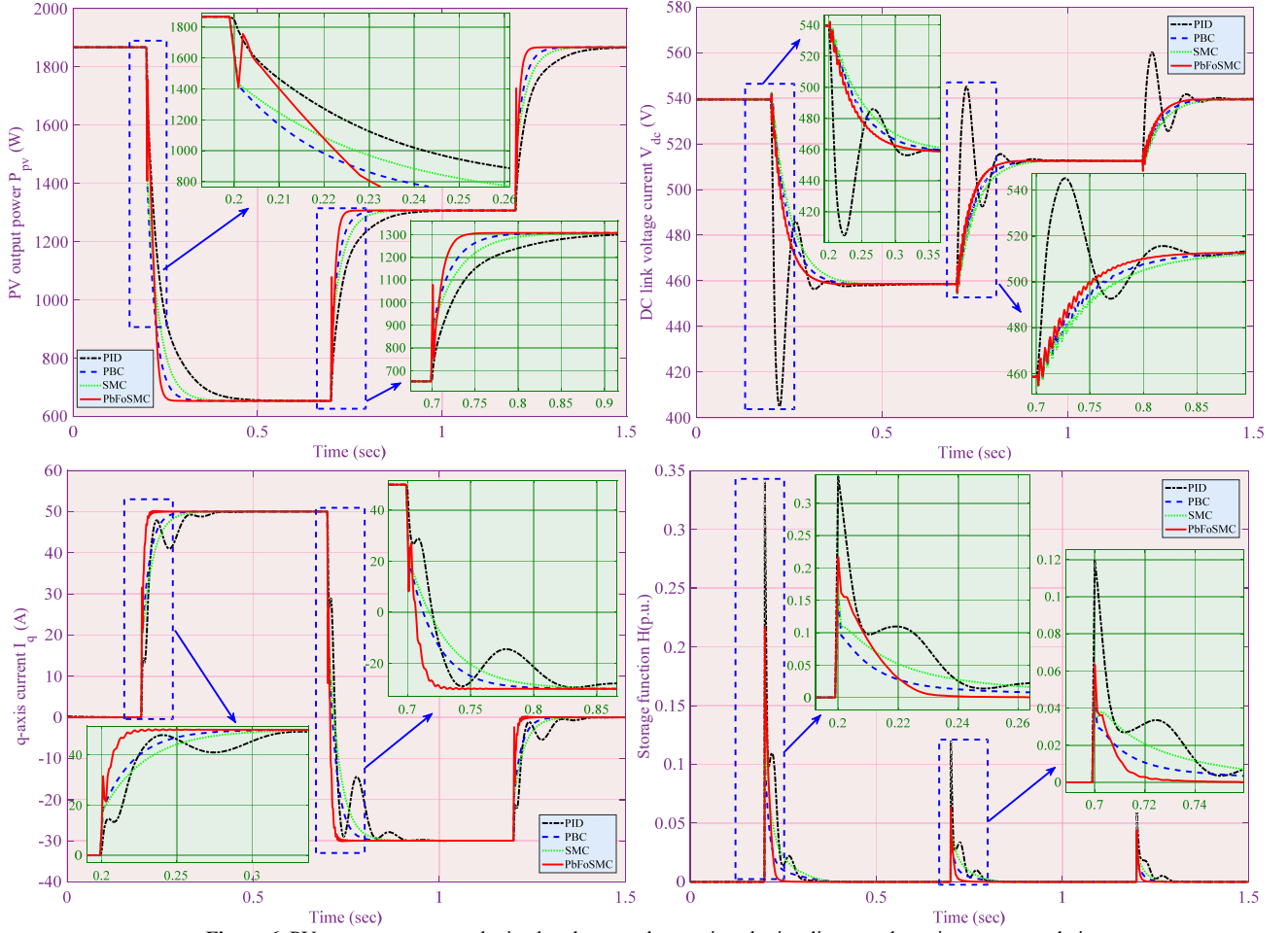
Table 2. The PbFoSMC parameters

q-axis current control	$\kappa_1 = 15$	$\varsigma_1 = 20$	$\varphi_1 = 35$	$\alpha_1 = 1.25$	$\lambda_{c1} = 25$	$\epsilon_{c1} = 0.15$
DC-link voltage control	$\kappa_2 = 25$	$\varsigma_2 = 30$	$\varphi_2 = 40$	$\alpha_2 = 1.75$	$\lambda_{c2} = 40$	$\epsilon_{c2} = 0.15$

### 5.1 Solar irradiance change

Three consecutive step changes in solar irradiance on which decrease from  $1 \text{ kW/m}^2$  to  $0.5 \text{ kW/m}^2$  at  $t=0.2 \text{ s}$ , increase to  $0.8 \text{ kW/m}^2$  at  $t=0.7 \text{ s}$ , and restores to  $1 \text{ kW/m}^2$  at  $t=1.2 \text{ s}$ , are studied, respectively. During the solar irradiance change, the temperature maintains at its rated value, e.g.,  $25^\circ\text{C}$ , together with q-axis current  $I_q$  being increased to  $50 \text{ A}$  at  $t=0.2 \text{ s}$ , decreased to  $-30 \text{ A}$  at  $t=0.7 \text{ s}$ , and restored to  $0 \text{ A}$  at  $t=1.2 \text{ s}$ . Figure 6 compares the corresponding PV system responses obtained under solar irradiance change. One can readily see that PID control brings in several DC-link voltage oscillations with large magnitude and overshoot due to its one-point linearization, which cannot achieve a consistent control performance under different operation conditions. In contrast, the other

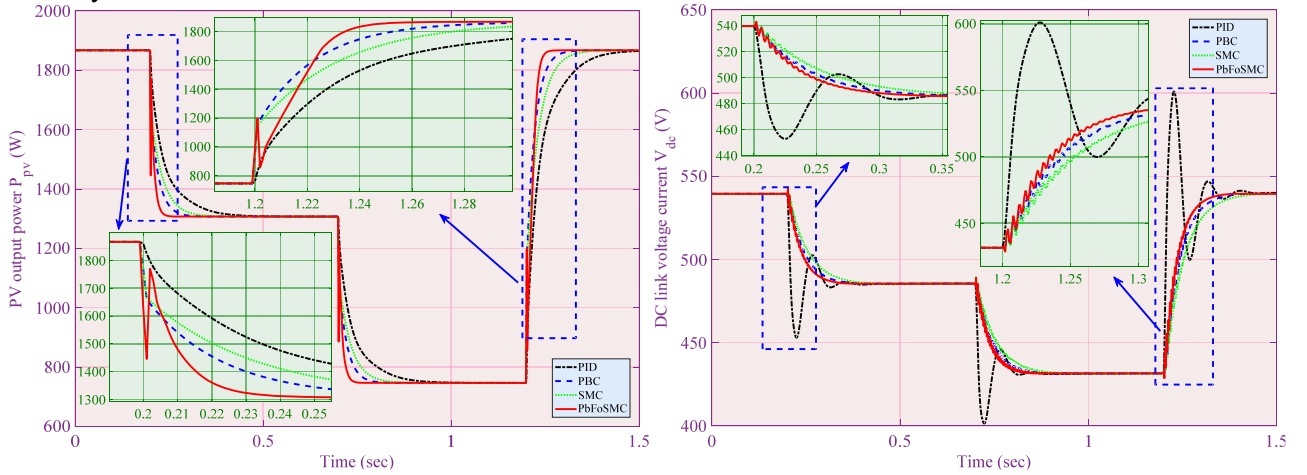
three controllers can realize a consistent control performance thanks to the cancellation of PV system nonlinearities. It is clear that PbFoSMC can offer the fastest tracking rate thanks to the combination of passivity and fractional-order sliding mode mechanism. Lastly, the real-time variation of storage function  $H(i_q, V_{dc}, I_{dc})$  demonstrates that PbFoSMC has the fastest tracking rate (steepest slope) and the lowest tracking error (lowest peak value).



**Figure 6.** PV system responses obtained under step changes in solar irradiance and q-axis current regulation.

## 5.2 Temperature variation

Three step changes of ambient temperature, e.g., increased from 25°C to 33°C and 40°C at  $t=0.2$  s and  $t=0.7$  s, then decreased from 40°C to 25°C at  $t=1.2$  s, are investigated. Meanwhile, the solar irradiance maintains to be 1 kW/m<sup>2</sup>, together with q-axis current  $I_q$  decreases to -40 A at  $t=0.2$  s, increases to 30 A at  $t=0.7$  s, and restores to 0 A at  $t=1.2$  s, respectively. The obtained PV system responses are illustrated in Fig. 7, which shows that PbFoSMC can achieve the most satisfactory control performance among four controllers as it can offer the highest tracking rate without any overshoot.



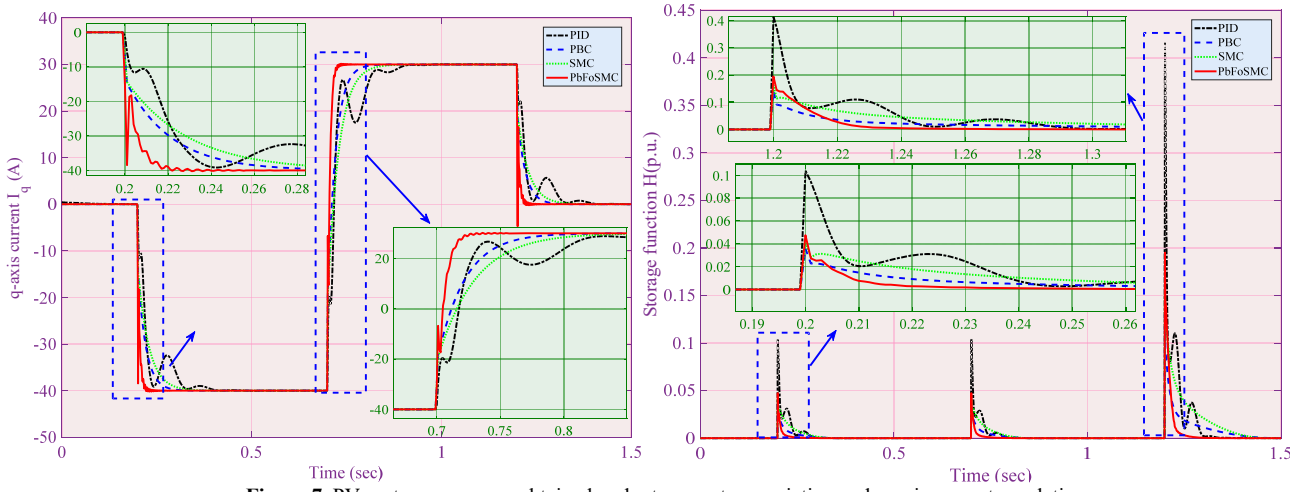


**Figure 7.** PV system responses obtained under temperature variation and q-axis current regulation.

### 5.3 Power grid voltage drop

Fault ride-through (FRT) requires the PV system to stay connected and contribute to the power grid in case of severe power grid voltage disturbances as the disconnection may further degrade the voltage restoration during and after the fault [33-35]. In order to test the FRT capability of the proposed approach, a power grid voltage drop to 0.4 p.u. for 150 ms ( $t=0.2s-0.35s$ ) [36] at the standard operation condition is applied. Figure 8 depicts the corresponding PV system responses. It can be observed that PbFoSMC is able to restore the active power, DC-link voltage, and q-axis current caused by the fault with the fastest rate and lowest oscillations. This can also be verified from the variation of the storage function, e.g. a minimal energy magnitude change and rapid energy dissipation could be obtained by PbFoSMC.

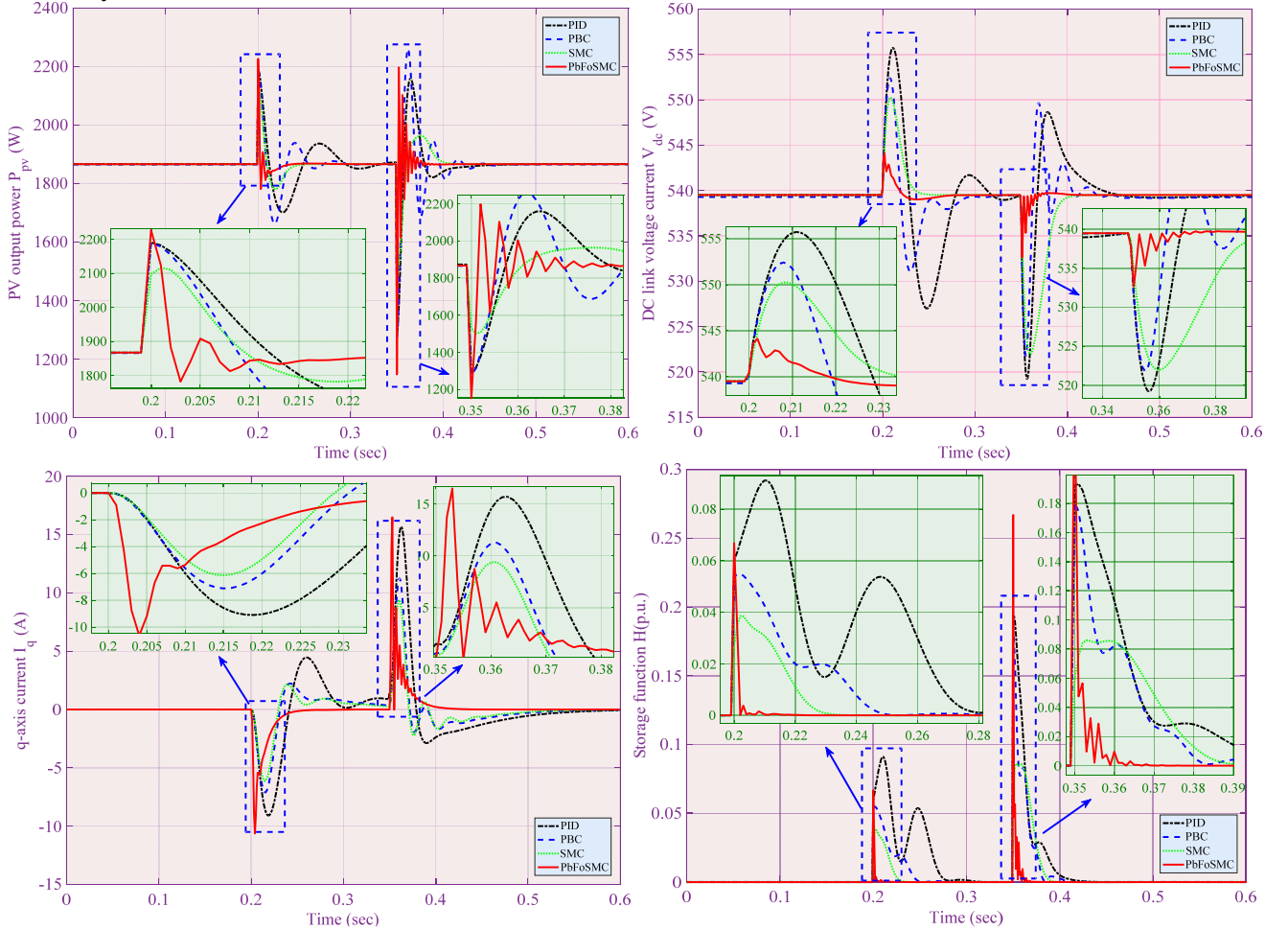


**Figure 8.** PV system responses obtained under the 60% voltage drop lasting 150 ms at power grid.

### 5.4 PV inverter parameter uncertainties

In practice, the accurate PV inverter parameters may not be obtained due to the inaccurate measurement, ambient temperature, air density, wear-and-error, etc. Therefore, it is of great importance to test the robustness of PbFoSMC

in the presence of PV inverter parameter uncertainties. Here, a series of plant-model mismatches of equivalent resistance  $R$  and inductance  $L$  associated with  $\pm 20\%$  variation around their rated value are applied, in which a 40% voltage drop lasting 100 ms at the power grid is adopted while the absolute peak value of active power  $|P|$  is recorded. Figure 9 compares the variation of the absolute peak value of active power  $|P|$  obtained by PID control, PBC, SMC, and PbFoSMC, which is 10.38%, 17.54%, 5.11%, and 4.87% under resistance uncertainties, respectively. As a result, PbFoSMC can provide considerable robustness against to PV inverter parameter uncertainties thanks to the exploitation of the beneficial terms and FoSMC.

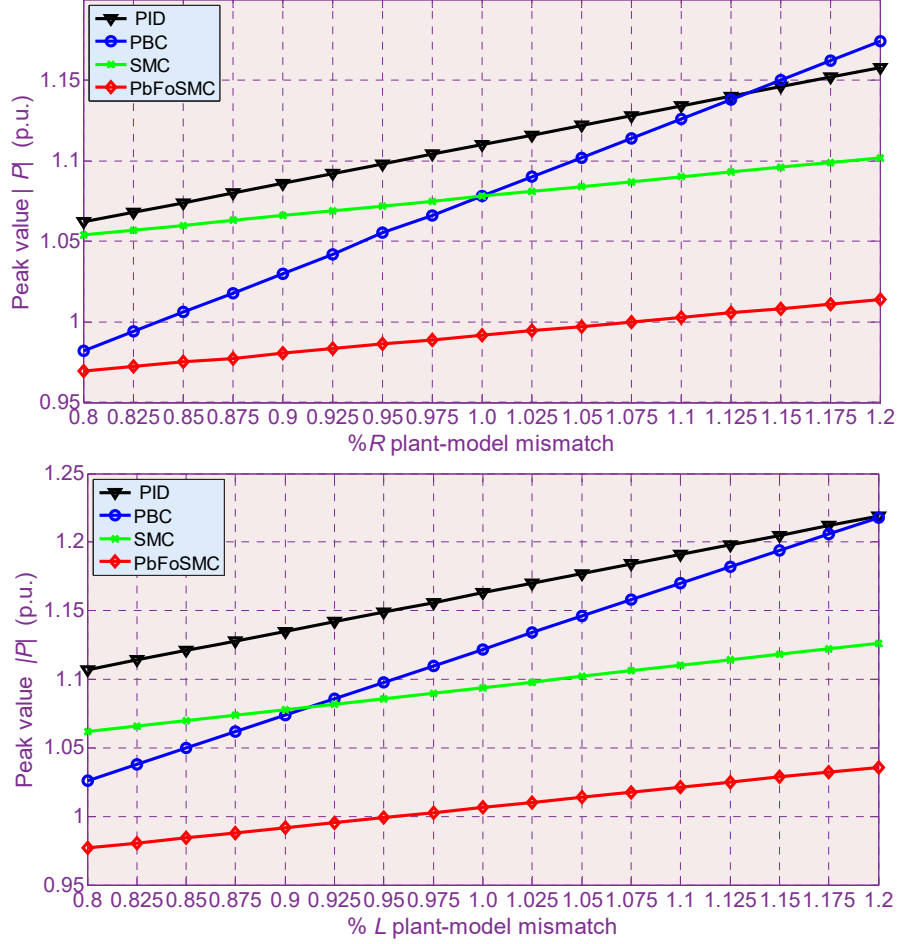


**Figure 9.** Absolute peak value of active power  $|P|$  obtained under a 40% voltage drop lasting 100 ms at power grid associated with  $\pm 20\%$  variation of the equivalent resistance  $R$  and inductance  $L$  of four controllers.

### 5.5 Comparative studies

The integral of absolute error (IAE) indices [37,38] of four controllers calculated in the above three cases are compared in Table 3 with  $IAE_x = \int_0^T |x - x^*| dt$ . The simulation time  $T=3$  s is chosen to consider the whole operation range of three cases. From Table 3, one can observe that PbFoSMC has the lowest IAE indices. Therefore, it outperforms other three controllers. Particularly, its  $IAE_{I_q}$  is merely 74.78%, 84.66%, and 82.88% of that of PID control, PBC, and SMC, in the solar irradiance change, respectively. Besides, its  $IAE_{V_{dc}}$  is only 82.56%, 90.54%, and 90.11% of that of PID control, PBC, and SMC, in the power grid voltage drop, respectively.

**Table 3** IAE indices (in p.u.) of four controllers obtained in three scenarios.

Scenarios	IAE Indices	PID	PBC	SMC	PbFoSMC
Solar irradiance change	$IAE_{I_q}$	0.1852	0.1636	0.1671	0.1385
	$IAE_{V_{dc}}$	0.4498	0.4378	0.4403	0.3867
Temperature variation	$IAE_{I_q}$	0.2233	0.2055	0.2092	0.1613
	$IAE_{V_{dc}}$	0.5604	0.5292	0.5325	0.4737
Power grid voltage drop	$IAE_{I_q}$	0.3448	0.2964	0.2997	0.2444
	$IAE_{V_{dc}}$	0.7557	0.6891	0.6924	0.6239

Besides, the overall storage function, e.g.,  $\int_0^T H(i_q, V_{dc}, I_{dc}) dt$ , obtained under three cases is illustrated in Fig. 10, which compares the accumulated energy of the PV system caused by the tracking error while a higher value represents a larger overall tracking error. It can be seen that PID control has the largest accumulated tracking error

among four controllers. In contrast, PbFoSMC owns the smallest accumulated tracking error thus it can achieve the most satisfactory control performance among all approaches.

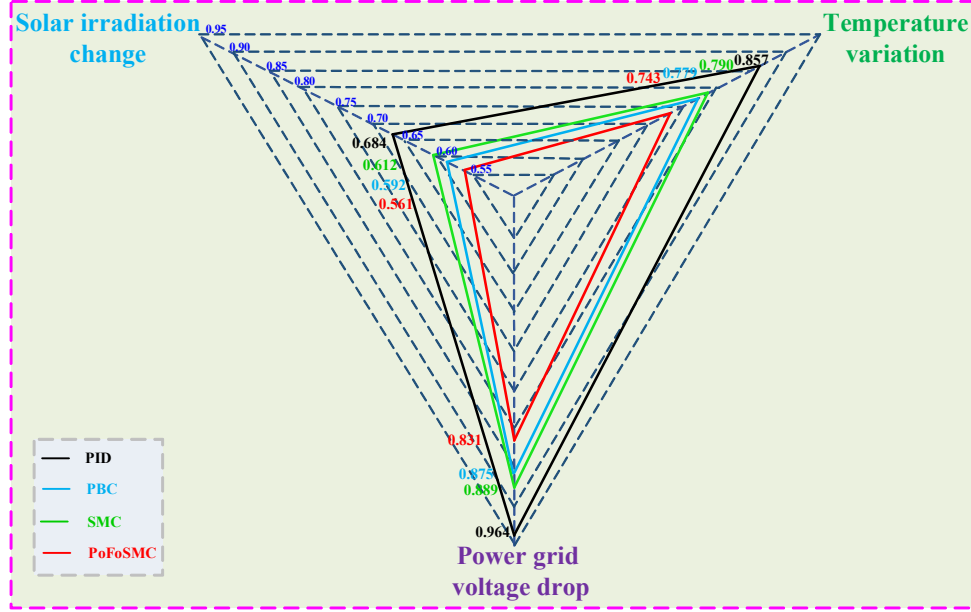


Figure 10. Radar diagram of the overall storage function of four controllers obtained in three cases.

Finally, the overall control costs, i.e.,  $\int_0^T (|u_1| + |u_2|) dt$  [39,40], of each controller needed in three cases are shown in Fig. 11. It demonstrates that PbFoSMC just requires the lowest overall control costs in all cases among all methods. In particular, in the temperature variation, its overall control costs are only 86.03%, 94.61%, and 96.29% to that of PID control, PBC, and SMC, respectively.

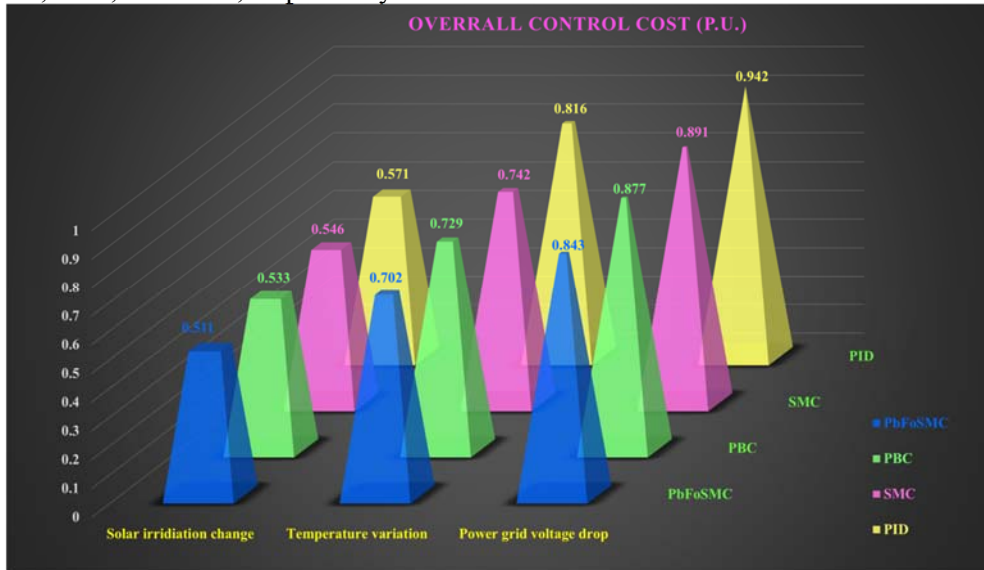


Figure 11. Overall control costs required by four controllers obtained under three cases.

## 6. HIL Test

Real-time digital simulation based high-fidelity modeling can give a close-to-reality representation of the system dynamic performance. In addition, real-time simulation speed can be reached. Such simulation model can be used for prototype operation and control tests [41]. It has been adopted to validate the implementation feasibility of different PV controllers systems [42,43]. Hence, this section undertakes a dSpace based HIL test to validate the hardware implementation feasibility of the proposed approach for PV inverters to achieve MPPT.

The configuration and experiment platform of the HIL test are demonstrated by Fig. 12 and Fig. 13, respectively. Here, PbFoSMC based q-axis current and DC-link voltage controller (28), (30) and (31) is implemented on DS1104 board with a sampling frequency  $f_c=1$  kHz. Meanwhile, the PV system is embedded on DS1006 board with a limit sampling frequency  $f_s=50$  kHz to make the HIL simulator as close to the real PV system as possible [44-46]. The measurements of the q-axis current  $i_q$  and DC-link voltage  $V_{dc}$  are obtained from the real-time calculation of the PV system on the DS1006 board, which are transmitted to PbFoSMC implemented on the DS1104 board for the real-time closed-loop system control.



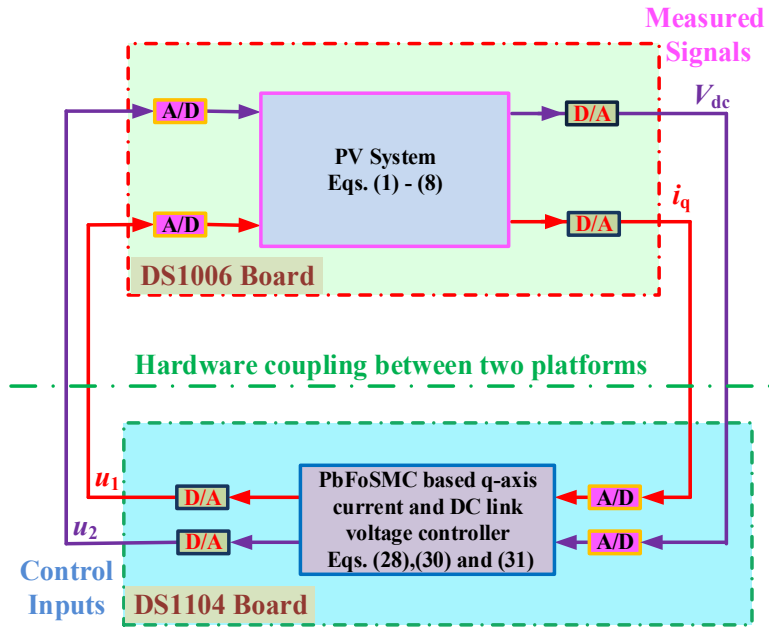


Figure 12. The schematic configuration of HIL experiment.

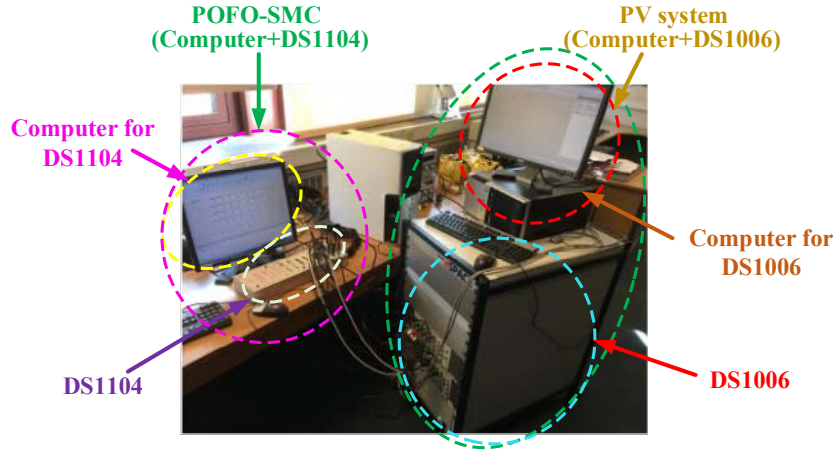
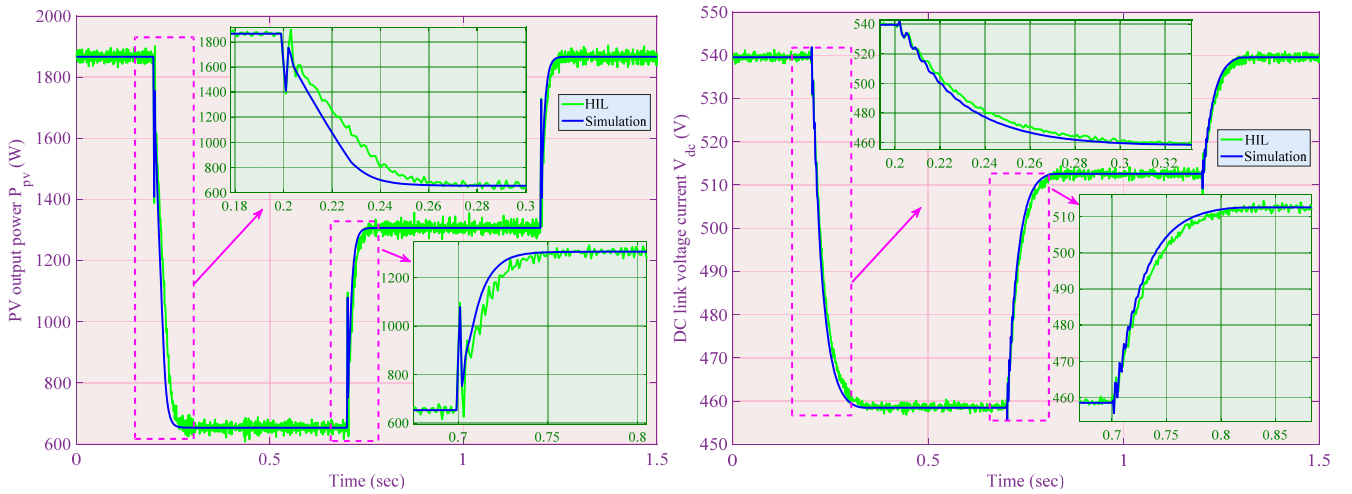


Figure 13. The hardware platform of HIL experiment.

### 6.1 HIL test results of solar irradiance change

The same solar irradiance change is applied and the obtained HIL test results are presented with simulation results. It can be seen from Fig. 14 that HIL test results is very close to the simulation results, which validates the implementation feasibility of PbFoSMC under solar irradiance change.





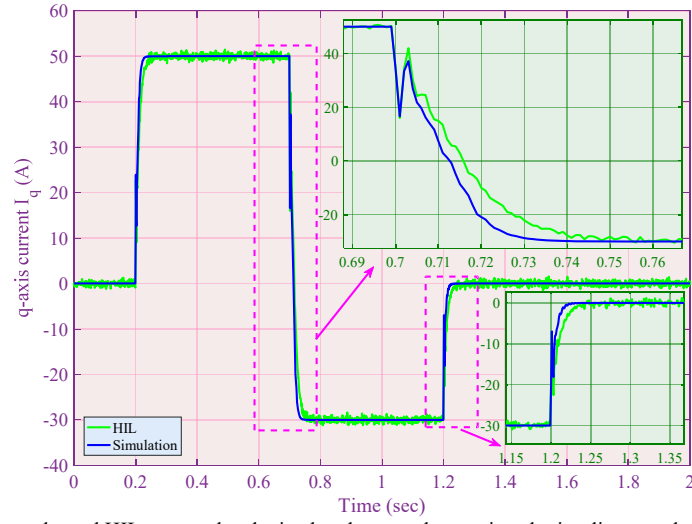


**Figure 14.** Simulation results and HIL test results obtained under step changes in solar irradiance and q-axis current regulation.

### 6.2 Temperature changes

Figure 15 illustrates the simulation results and HIL test results obtained under the temperature changes. One can readily find that the HIL test results could match the simulation results very well.

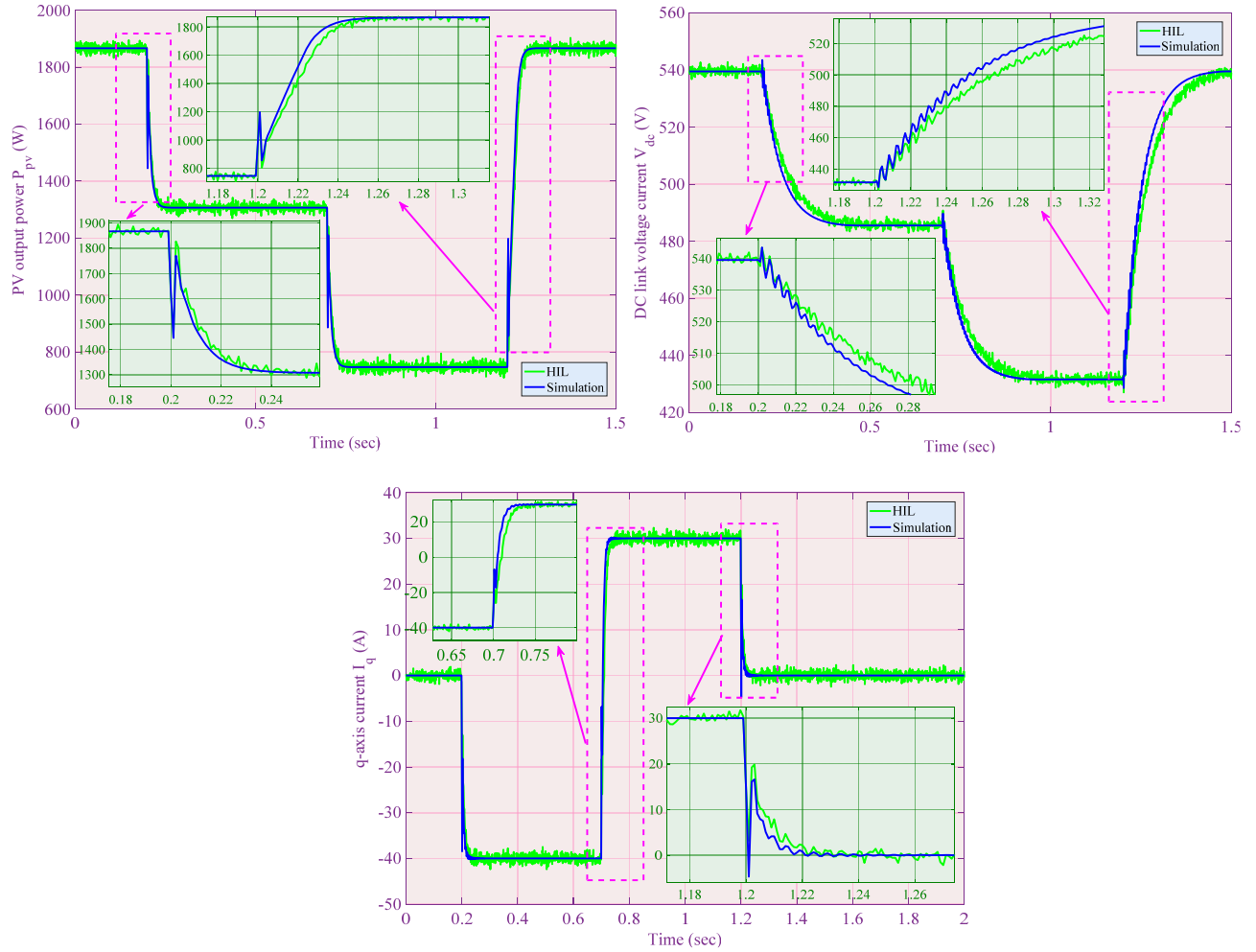


**Figure 15.** Simulation results and HIL test results obtained under temperature variation and q-axis current regulation.

### 6.3 Power grid voltage drop

The simulation results and HIL test results obtained under power grid voltage drop are compared in Fig. 16, from which it could be easily found that their curves are very similar.

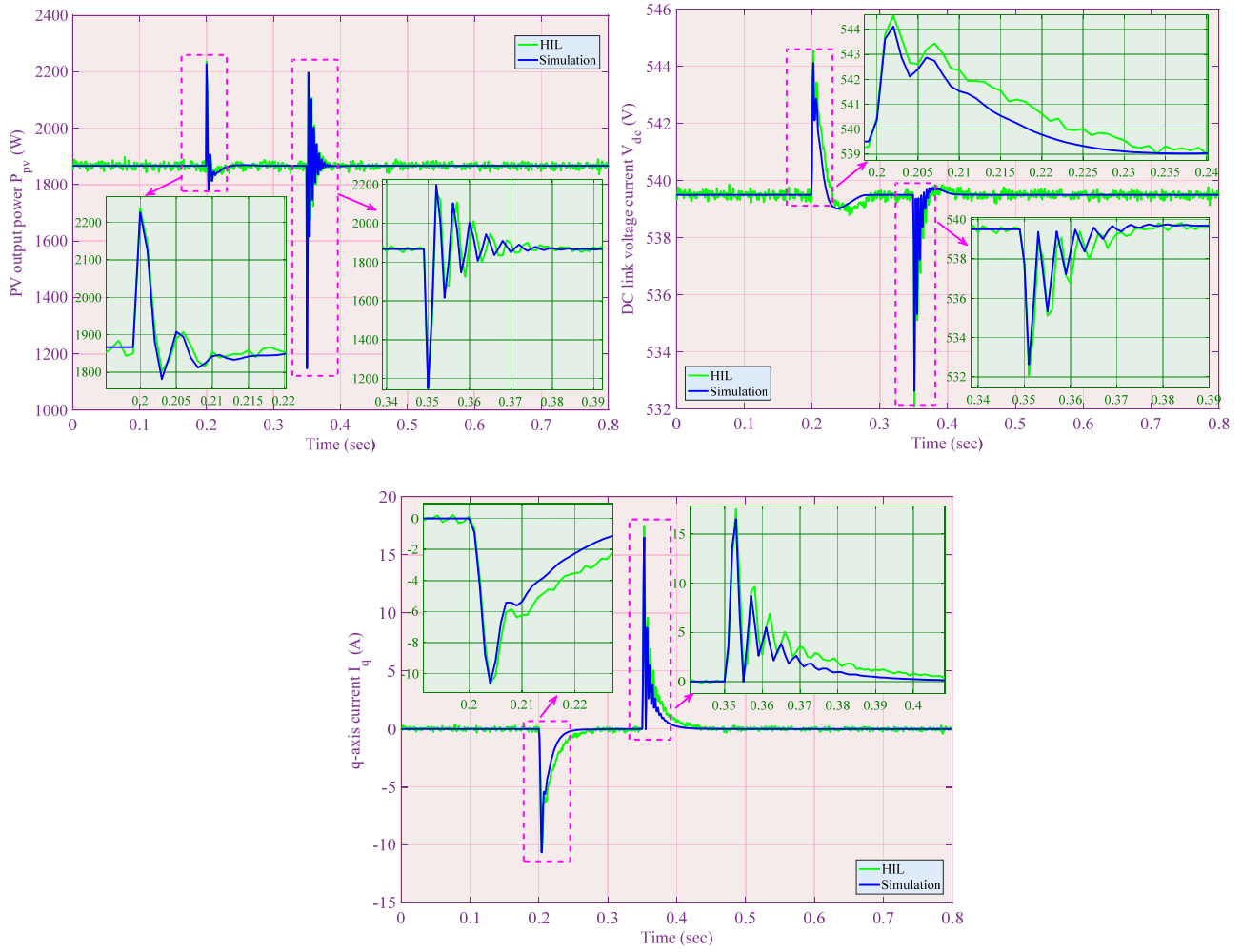


**Figure 16.** Simulation results and HIL test results obtained under power grid voltage drop.

Finally, the differences between the simulation results and the HIL test results are mainly due to the following three reasons:

- *Measurement errors and noises:* They are ubiquitously existed in the HIL test which usually lead to a consistent oscillation of the HIL test results. A filter could be employed to dramatically attenuate such oscillations to improve the control performance;
- *Different sampling frequency:* The sampling frequency of the PV system and controller is the same in the simulation, however it is different in the HIL test. Such sampling frequency difference would cause the simulation results to be unmatched to the HIL test;
- *Time delay:* There exists some time delay in the HIL test which is however not considered in the simulation.

## 7. Conclusions

In this paper, a novel PbFoSMC scheme is proposed for a grid-connected PV inverter to harvest the available maximum solar energy under various operation conditions. The conclusions can be summarized as follows:

- (1) Based on the passivity theory, a storage function associated with DC-link voltage and DC-link current, as well as q-axis current is constructed for the PV system, in which the physical characteristics of each term is thoroughly investigated and analyzed. Then, the beneficial terms are carefully retained and fully exploited for the control performance improvement of the closed-loop system;
- (2) FoSMC framework is synthesized as an additional input for the passivized system, which can desirably reshape the retained energy of the storage function and considerably enhance the robustness;
- (3) Simulation results of case studies demonstrate that PbFoSMC can outperform PID control, PBC, and SMC under various atmospheric conditions with fastest tracking rate, smallest overshoot, and lowest control costs;
- (4) dSpace based HIL test validates the implementation feasibility of the proposed approach.

## Acknowledgments

The authors gratefully acknowledge the support of National Natural Science Foundation of China (51477055, 51667010, 51777078).

## References

- [1] Yang, B.; Yu, T.; Shu, H. C.; Dong, J.; Jiang, L. Robust sliding-mode control of wind energy conversion systems for optimal power extraction via nonlinear perturbation observers. *Applied Energy* **2018**, 210: 711-723.
- [2] Wang, W.Y.; Yu, N.P.; Johnson R. A model for commercial adoption of photovoltaic systems in California. *Journal of Renewable and Sustainable Energy* **2017**, 9, 025904.
- [3] Yang, B.; Jiang, L.; Wang, L.; Yao, W.; Wu, Q.H. Nonlinear maximum power point tracking control and modal analysis of DFIG based wind turbine. *International Journal of Electrical Power & Energy Systems* **2016**, 74: 429-436.
- [4] Al-Douri, Y.; Abed, F.M. Solar energy status in Iraq: Abundant or not-Steps forward. *Journal of Renewable and Sustainable Energy* **2016**, 8, 025905.
- [5] Shen, Y.; Yao, W.; Wen, J.Y.; He, H.B. Adaptive wide-area power oscillation damper design for photovoltaic plant considering delay compensation. *IET Generation, Transmission and Distribution* **2017**, 11(18), 4511-4519.
- [6] Kandemir, E.; Cetin, N.S.; Borekci, S. A comprehensive overview of maximum power extraction methods for PV systems. *Renewable and Sustainable Energy Reviews* **2017**, 78: 93-112.
- [7] Tanaka, T.; Toumuya, T.; Suzuki, T. Output control by hill-climbing method for a small scale wind power generating system. *Renewable Energy* **2014**, 12(4): 387-400.
- [8] Mohanty, S.; Subudhi, B.; Ray, P.K. A grey wolf-assisted Perturb & Observe MPPT algorithm for a PV system. *IEEE Transactions on Energy Conversion* **2017**, 32(1): 340-347.
- [9] Zakzouk, N.E.; Elshaharty, M.A.; Abdelsalam, A.K.; Helal, A.A. Improved performance low-cost incremental conductance PV MPPT technique. *IET Renewable Power Generation* **2016**, 10(4): 561-574.
- [10] Kadri, R.; Gaubert, J.P.; Champenois, G. An improved maximum power point tracking for photovoltaic grid-connected inverter based on voltage-oriented control. *IEEE Transactions on Industrial Electronics* **2011**, 58(1): 66-75.
- [11] Mitkowski, W.; Oprzedkiewicz, K. Tuning of the half-order robust PID controller dedicated to oriented PV system. *Lecture Notes in Electrical Engineering* **2015**, 320: 145-157.
- [12] Ramadan, H.S. Optimal fractional order PI control applicability for enhanced dynamic behavior of on-grid solar PV systems. *International Journal of Hydrogen Energy* **2017**, 42(7): 4017-4031.
- [13] Lalili, D.; Mellit, A.; Lourci, N.; Medjahed, B. Berkouk, E.M. Input output feedback linearization control and variable step size MPPT algorithm of a grid-connected photovoltaic inverter. *Renewable Energy* **2011**, 36: 3282-3291.
- [14] Lalili, D.; Mellit, A.; Lourci, N.; Medjahed, B.; Boubakir, C. State feedback control and variable step size MPPT algorithm of three-level grid-connected photovoltaic inverter. *Solar Energy* **2013**, 98: 561-571.
- [15] Naghmasha, Armghan, H.; Ahmad, I.; Armghan, A.; Khan, S.; Arsalan, Muhammad. Backstepping based non-linear control for maximum power point tracking in photovoltaic system. *Solar Energy* **2018**, 159: 134-141.
- [16] Shadmand, M.B.; Balog, R.S.; Abu-Rub, H. Model predictive control of PV sources in a smart DC distribution system: maximum power point tracking and droop control. *IEEE Transactions on Energy Conversion* **2014**, 29(4): 913-921.
- [17] Kumar, N.; Saha, T.K.; Dey, J. Sliding mode control, implementation and performance analysis of standalone PV fed dual inverter. *Solar Energy* **2017**, 155:1178-1187.
- [18] Mohomad, H.; Saleh, S.A.M.; Chang, L. Disturbance estimator-based predictive current controller for single-phase interconnected PV systems. *IEEE Transactions on Industry Applications* **2017**, 53(5): 4201-4209.
- [19] Ortega, R.; Schaft, A.; Mareels, I.; Maschke, B. Putting energy back in control. *IEEE Control Systems* **2001**, 21(2): 18-33.
- [20] Ortega, R.; Schaf, A.; Castanos, F.; Astolfi, A. Control by interconnection and standard passivity-based control of port-Hamiltonian systems. *IEEE Transactions on Automatic Control* **2008**, 53(11): 2527-2542.
- [21] Bao, X.; Wang, J.; Xiang, H.; Ma, Y. The maximum power point tracking technology of passivity-based photovoltaic grid-connected system. IEEE 7th International Power Electronics and Motion Control Conference-ECCE Asia, June 2-5, 2012, Harbin, China, p. 1372-1376.
- [22] Tofighi, A.; Kalantar, M. Power management of PV/battery hybrid power source via passivity-based control. *Renewable Energy* **2011**, 36(9): 2440-2450.
- [23] Mojallizadeh, M.R.; Badamchizadeh, M.A. Adaptive passivity-based control of a photovoltaic/battery hybrid power source via algebraic parameter identification. *IEEE Journal of Photovoltaics* **2016**, 6(2): 532-539.
- [24] Wang, J.; Mu, X.; Li, Q.K. Study of passivity based decoupling control of T-NPC PV grid-connected inverter. *IEEE Transactions on Industrial Electronics* **2017**, 64(9):7542-7551.
- [25] Biel, D.; Scherpen, J.M.A. Passivity-based control of active and reactive power in single-phase PV inverters. IEEE International Symposium on Industrial Electronics, 19-21 June, 2017, Edinburgh, UK, p. 999-1004.
- [26] Zhang, B.T.; Pi, Y.G.; Luo, Y. Fractional order sliding-mode control based on parameters auto-tuning for velocity control of permanent magnet synchronous motor. *ISA Transactions* **2012**, 51(5): 649-656.
- [27] Tang, Y.; Zhang, X.; Zhang, D.; Zhao, G.; Guan, X. Fractional order sliding mode controller design for antilock braking systems. *Neurocomputing* **2013**, 111(6), 122-130.
- [28] Yang, B.; Yu, T.; Shu, H.C.; Zhu, D.N.; An, N.; Sang, Y.Y.; Jiang, L. Energy reshaping based passive fractional-order PID control design of a grid-connected photovoltaic inverter for optimal power extraction using grouped grey wolf optimizer. *Solar Energy* **2018**, 170: 31-46.
- [29] Yang, B.; Yu, T.; Shu, H.C.; Zhu, D.N.; Zeng, F.; Sang, Y.Y.; Jiang, L. Perturbation observer based fractional-order PID control of photovoltaics inverters for solar energy harvesting via Yin-Yang-Pair optimization. *Energy Conversion and Management* **2018**, 171: 170-187.
- [30] Podlubny, I. Fractional differential equations, Academic Press, New York, 1999.
- [31] Bharatiraja, C.; Jeevananthan, S.; Latha, R. FPGA based practical implementation of NPC-MLI with SVPWM for an autonomous operation PV system with capacitor balancing. *International Journal of Electrical Power & Energy Systems* **2014**, 61: 489-509.

- [32] Dhoke, A.; Sharma, R.; Saha, T.K. PV module degradation analysis and impact on settings of overcurrent protection devices. *Solar Energy* **2018**, 160: 360-367.
- [33] Wang, Y.; Ren, B. Fault ride-through enhancement for grid-tied PV systems with robust control. *IEEE Transactions on Industrial Electronics* **2018**, 65(3): 2302-2312.
- [34] Liao, S.W.; Yao, W.; Han, X.N.; Wen, J.Y.; Cheng, S.J. Chronological operation simulation framework for regional power system under high penetration of renewable energy using meteorological data. *Applied Energy* **2017**, 203: 816-828.
- [35] Liu, J.; Wen, J.Y.; Yao, W.; Long, Y. Solution to short-term frequency response of wind farms by using energy storage systems. *IET Renewable Power Generation* **2016**, 10(5): 669-678.
- [36] Tang, C.Y.; Chen, Y.T.; Chen, Y.M. PV power system with multi-mode operation and low-voltage ride-through capability. *IEEE Transactions on Industrial Electronics* **2015**, 62(12):7524-7533.
- [37] Yao, W.; Jiang, L.; Wen, J.Y.; Wu, Q.H.; Cheng, S.J. Wide-area damping controller for power system inter-area oscillations: a networked predictive control approach. *IEEE Transactions on Control Systems Technology* **2015**, 23(1), 27-36.
- [38] Shen, Y.; Yao, W.; Wen, J.Y.; He, H.B.; Chen, W.B. Adaptive supplementary damping control of VSC-HVDC for interarea oscillation using GrHDP. *IEEE Transactions on Power Systems* **2018**, 33(2), 1777-1789.
- [39] Yang, B.; Zhang, X.S.; Yu, T.; Shu, H.C.; Fang, Z.H. Grouped grey wolf optimizer for maximum power point tracking of doubly-fed induction generator based wind turbine. *Energy Conversion and Management* **2017**, 133, 427-443.
- [40] Yang, B.; Yu, T.; Shu, H.C.; Zhang, X.S.; Qu, K.P.; Jiang, L. Democratic joint operations algorithm for optimal power extraction of PMSG based wind energy conversion system, *Energy Conversion and Management* **2018**, 159, 312-326.
- [41] Tremblay, O.; Fortin-Blanchette, H.; Gagnon, R.; Brissette, Y. Contribution to stability analysis of power hardware-in-the-loop simulators. *IET Generation Transmission & Distribution* **2017**, 11(12): 3073-3079.
- [42] Mai, X.H.; Kwak, S.K.; Jung, J.H.; Kim, K.A. Comprehensive electric-thermal photovoltaic modeling for power-hardware-in-the-loop simulation (PHILS) applications. *IEEE Transactions on Industrial Electronics* **2017**, 64(8): 6255-6264.
- [43] Khazaei, J.; Miao, Z.; Piyasinghe, L.; Fan, L. Real-time digital simulation-based modeling of a single-phase single-stage PV system. *Electric Power Systems Research* **2015**, 123:85-91.
- [44] Yang, B.; Yu, T.; Shu, H.C.; Zhang, Y.M.; Chen, J.; Sang, Y.Y.; Jiang, L. Passivity-based sliding-mode control design for optimal power extraction of a PMSG based variable speed wind turbine, *Renewable Energy* **2018**, 119: 577-589.
- [45] Yang, B.; Sang, Y.Y.; Shi, K.; Yao, W.; Jiang, L.; Yu, T. Design and real-time implementation of perturbation observer based sliding-mode control for VSC-HVDC systems. *Control Engineering Practice* **2016**, 56: 13-26.
- [46] Yang, B.; Jiang, L.; Yao, W.; Wu, Q.H. Perturbation estimation based coordinated adaptive passive control for multimachine power systems. *Control Engineering Practice* **2015**, 44: 172-192.